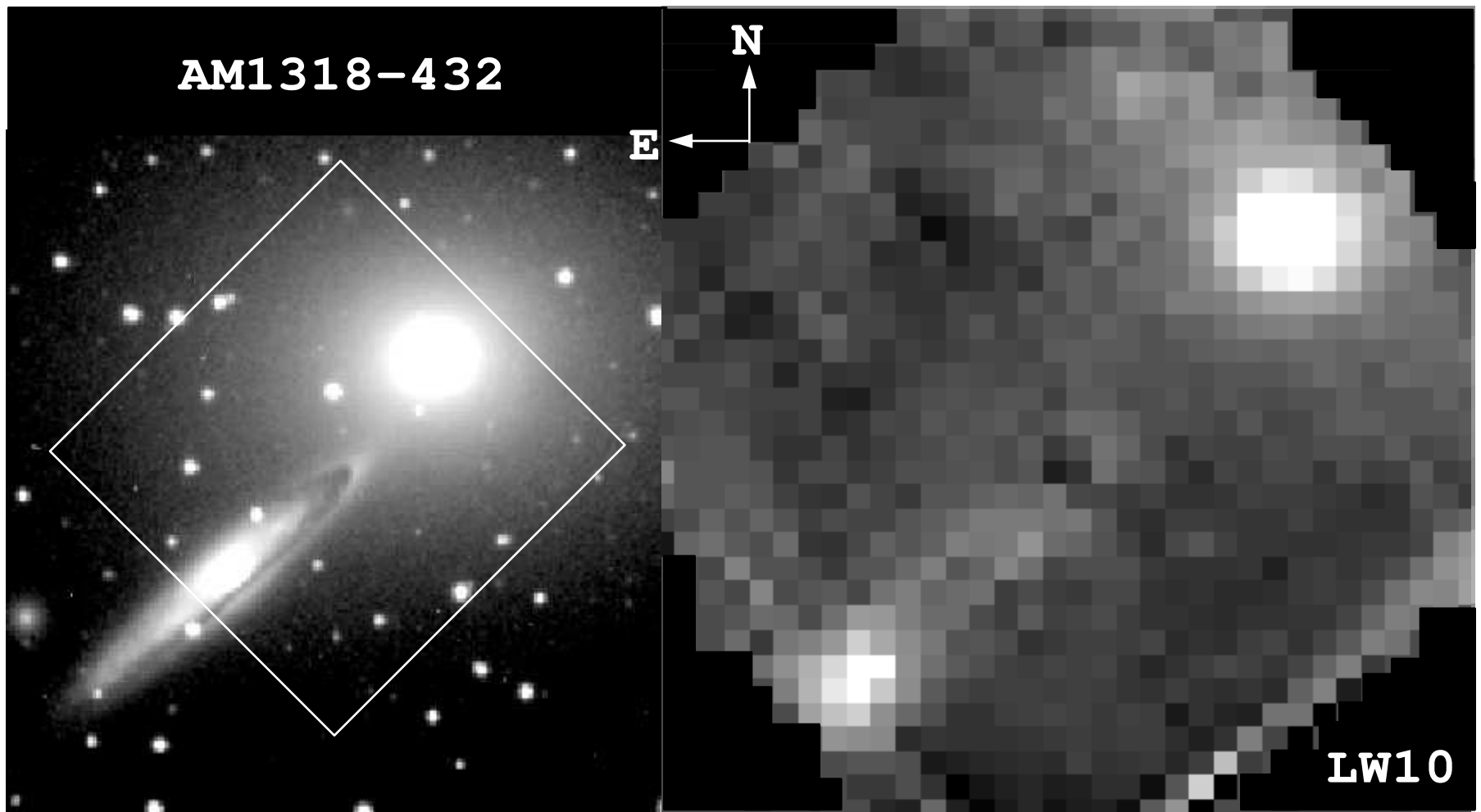
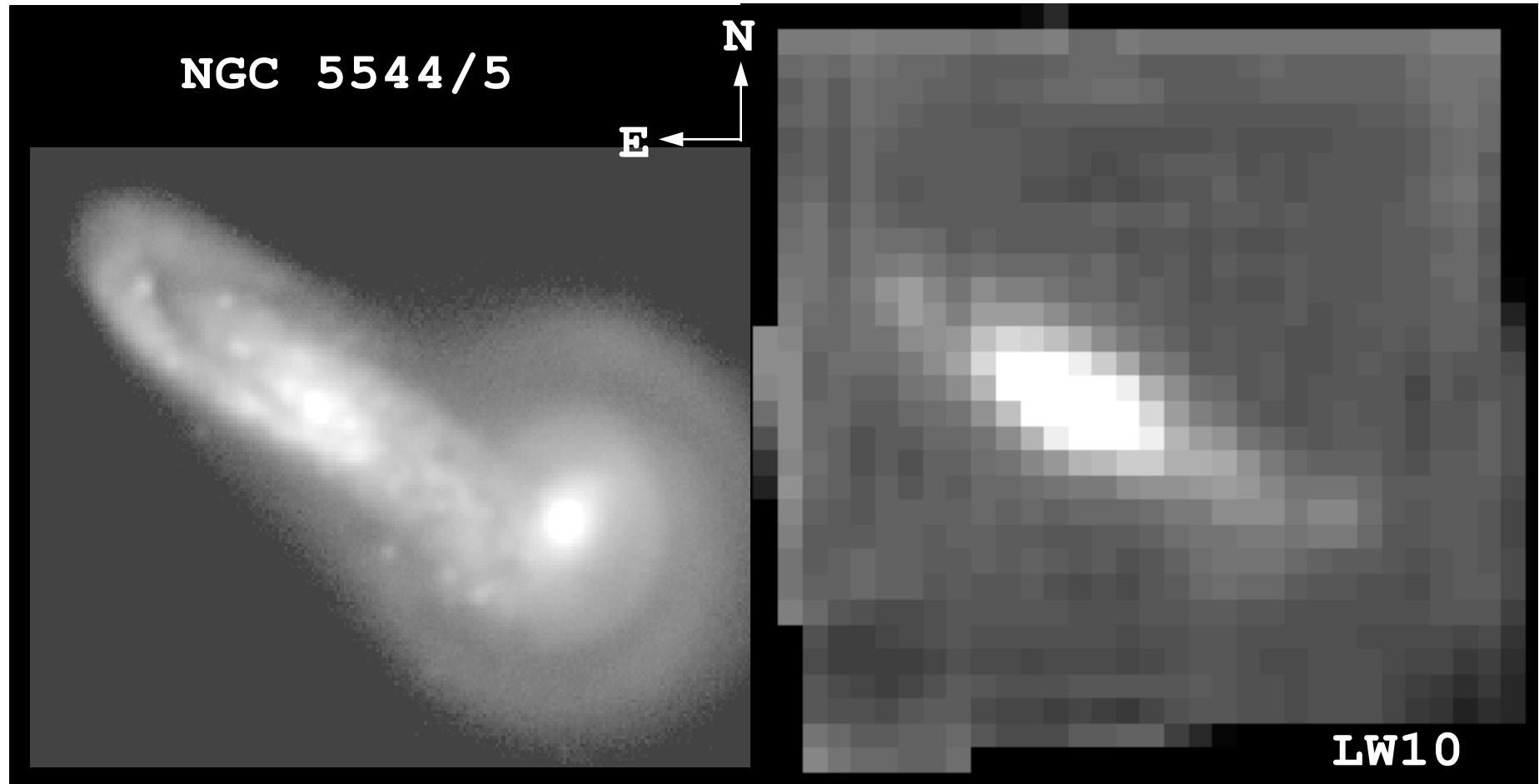


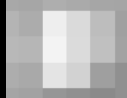
AM1318-432



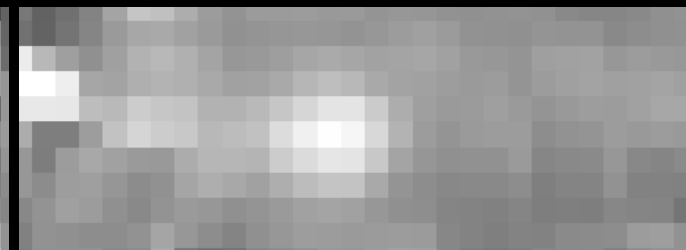
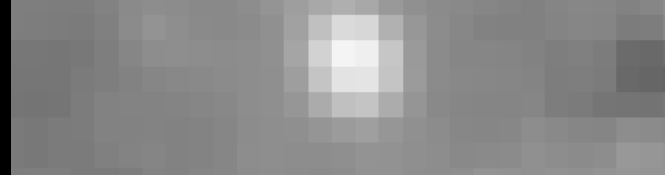


ISOPHOT Maps

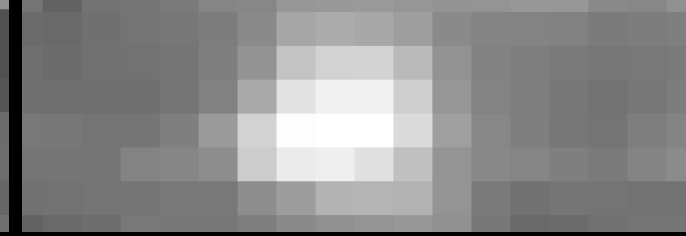
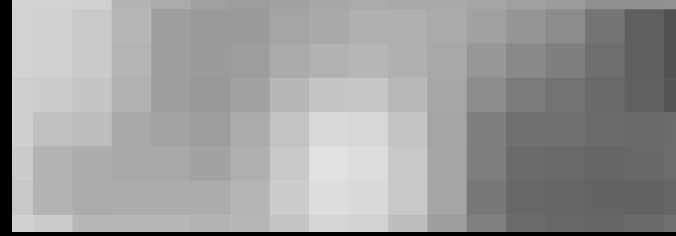
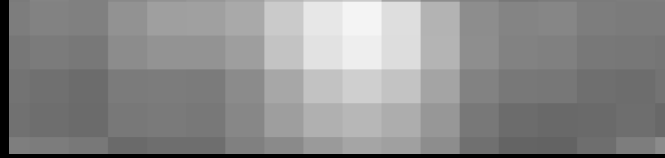
50 μ m



100 μ m



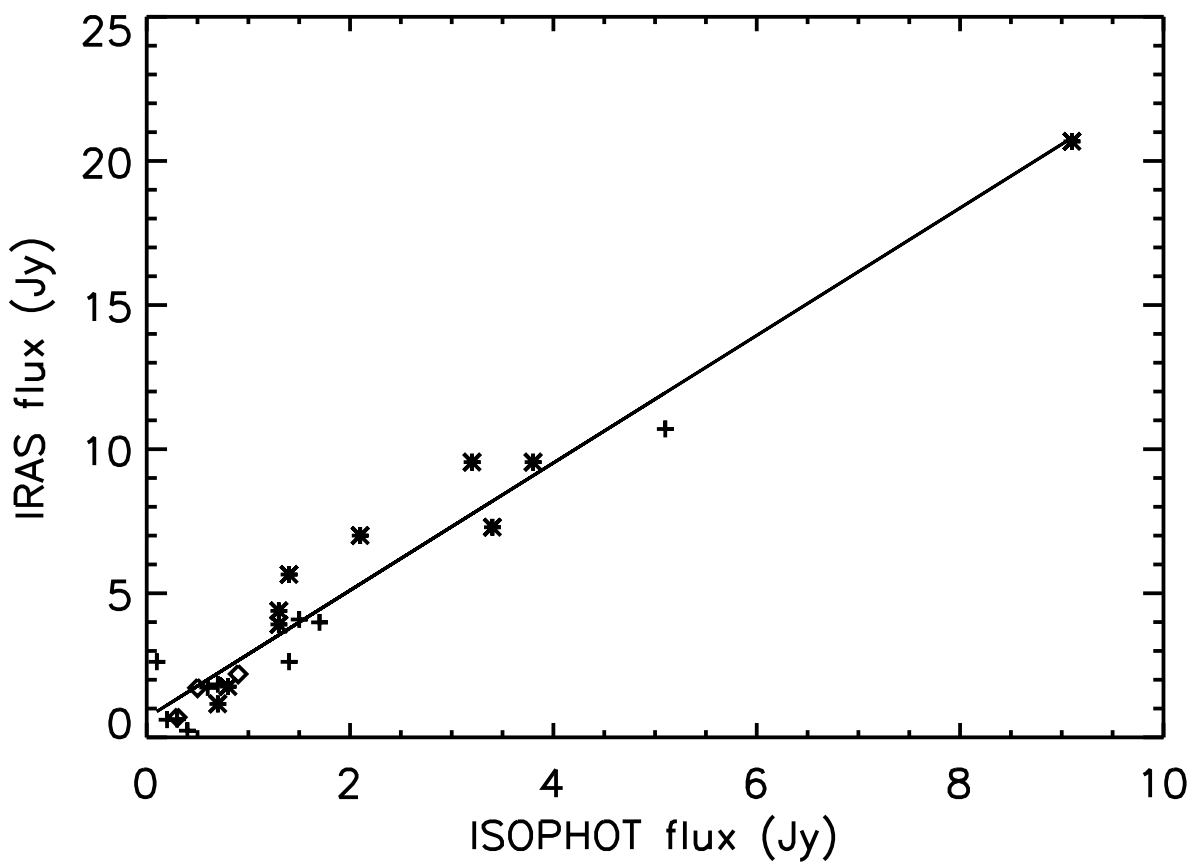
200 μ m

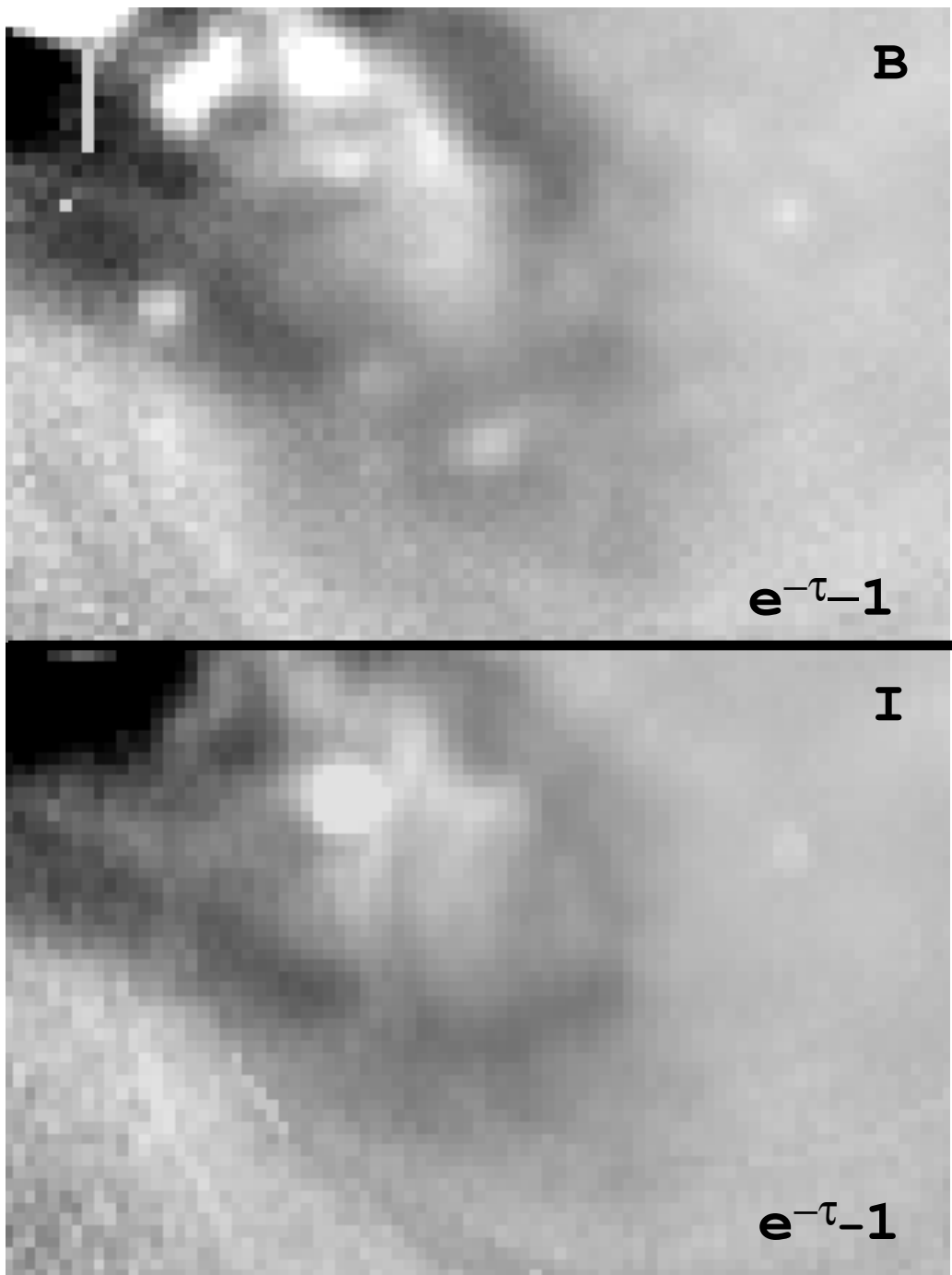


AM1316-241

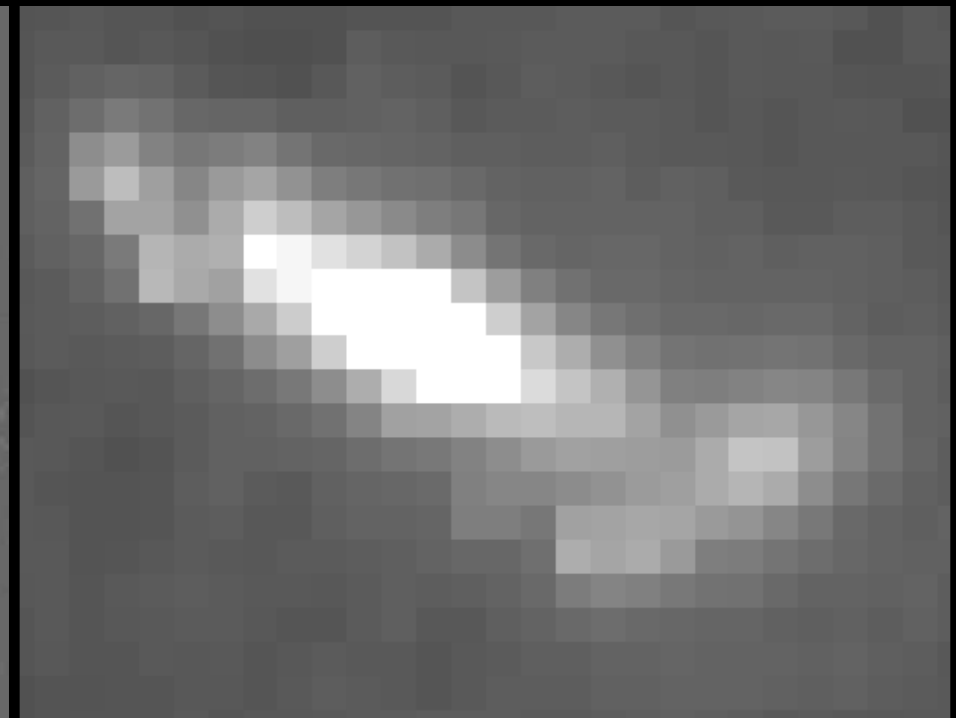
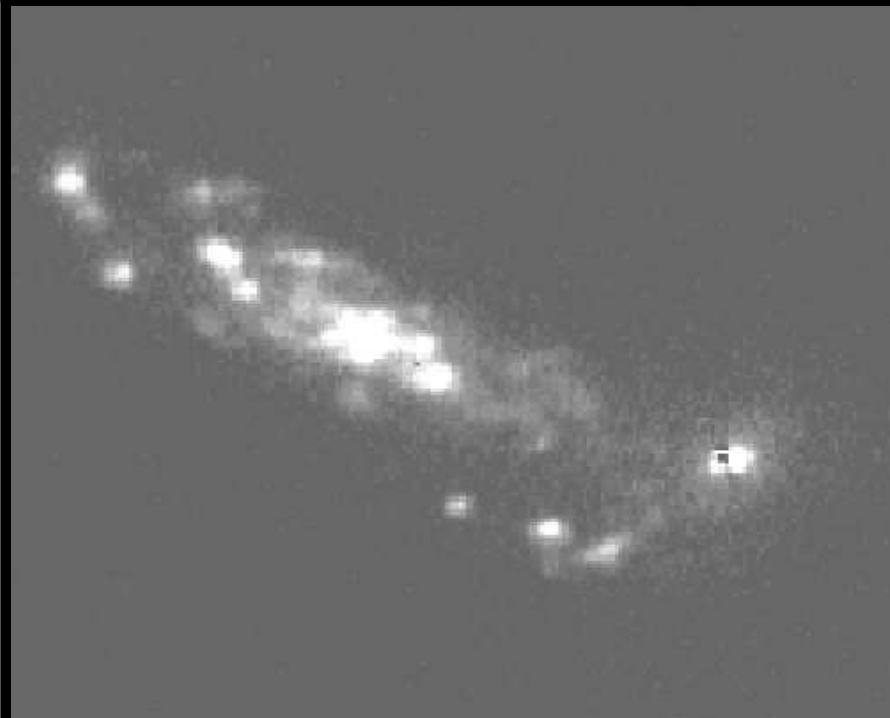
AM1318-432

NGC 5544/5





NGC 5544/5

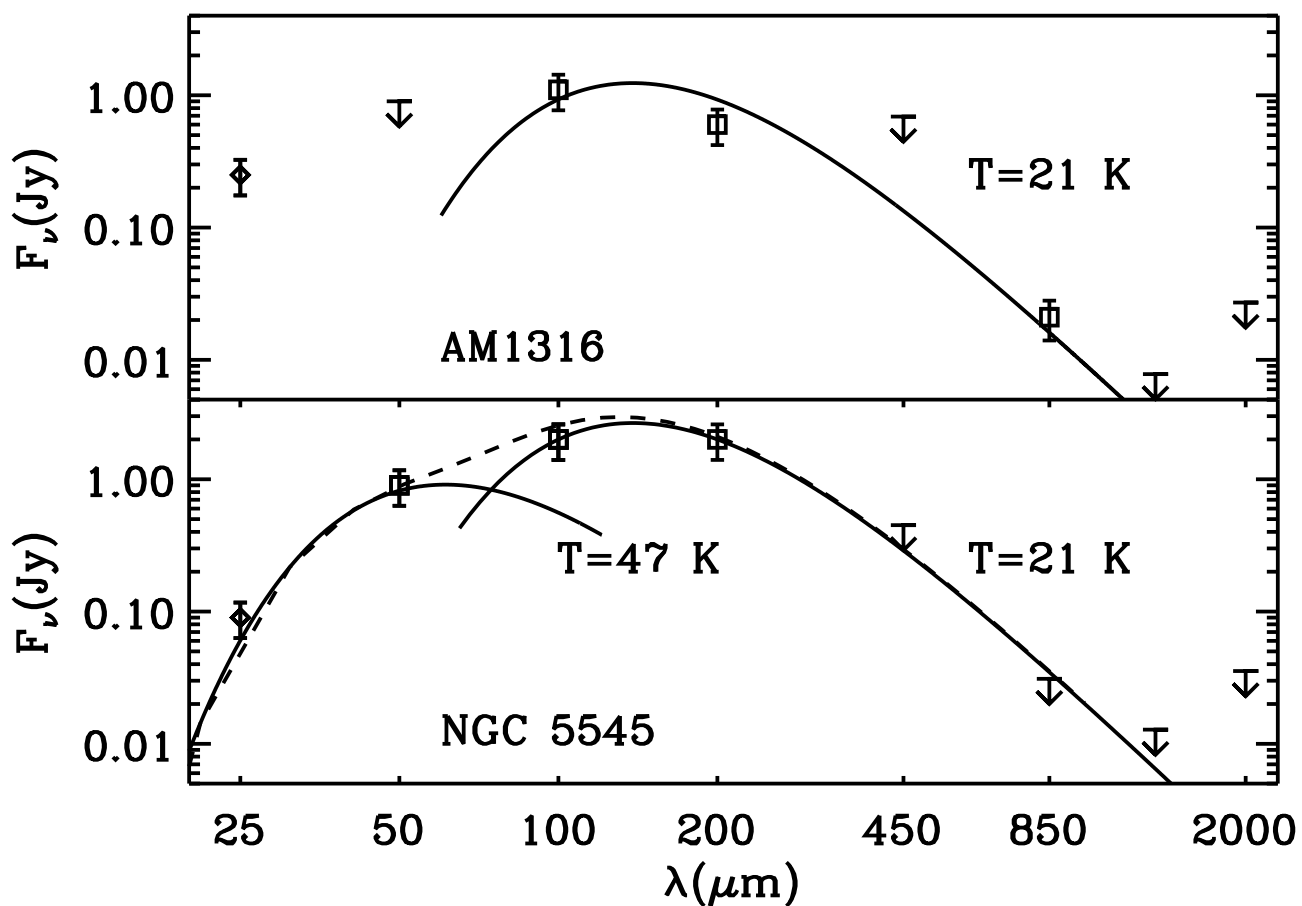


$\text{H}\alpha + [\text{NII}]$

$\text{H}\alpha + [\text{NII}]$
convolved
to LW10
PSF

ISOCAM
LW10

18"



Dust in Spiral Galaxies: Comparing Emission and Absorption to Constrain Small-Scale and Very Cold Structures¹

Donovan L. Domingue & William C. Keel^{2,3}

Department of Physics and Astronomy, University of Alabama, Box 870324, Tuscaloosa,
AL 35487-0324

Stuart D. Ryder

Joint Astronomy Centre, 660 N. A'ohoku Place, Hilo, HI 96720

Raymond E. White III³

Department of Physics and Astronomy, University of Alabama, Box 870324, Tuscaloosa,
AL 35487-0324

ABSTRACT

The detailed distribution of dust in the disks of spiral galaxies is important to understanding the radiative transfer within disks, and to measuring overall dust masses if significant quantities of dust are either very opaque or very cold. We address this issue by comparing measures of dust *absorption*, using the galaxy-overlap technique in the optical, with measures of the dust grains' thermal *emission* from 50-2000 μm using ISOPHOT on board ISO and SCUBA at the JCMT. We examine three spiral galaxies projected partially in front of E/S0 galaxies — AM1316-241, NGC 5545, and NGC 5091 (for NGC 5091 we have only optical and ISO data). Adopting an empirical exponential model for the dust distribution, we compare column densities and dust masses derived from the absorption and emission techniques. This comparison is sensitive to the amount of dust mass in small, opaque structures, which would not contribute strongly to area-weighted absorption measures, and to very cold dust, which would contribute to optical absorption but provide only a small fraction of the

¹Based on observations with ISO, an ESA project with instruments funded by ESA Member States (especially the PI countries: France, Germany, the Netherlands and the United Kingdom) with the participation of ISAS and NASA.

²Visiting astronomer, Kitt Peak National Observatory, National Optical Astronomy Observatories, operated by AURA, Inc., under cooperative agreement with the National Science Foundation.

³Visiting astronomer, Cerro Tololo Interamerican Observatory, National Optical Astronomy Observatories, operated by AURA, Inc., under cooperative agreement with the National Science Foundation.

sub-mm emission. In AM1316-241, we find global dust masses of $2 - 5 \times 10^7 M_{\odot}$, both techniques agreeing at the 50% level. NGC 5545 has about half this dust mass. The concordance of dust masses is well within the errors expected from our knowledge of the radial distribution of dust, and argues against any dominant part of the dust mass being so cold or opaque.

The 50-2000 μm data are well fitted by modified Planck functions with an emissivity law $\beta = -2$, at 21 ± 2 K; a modest contribution from warmer dust is required to fit only the 50 μm measurement of NGC 5545. We incorporate empirical corrections to the flux scale of ISOPHOT P32 data, which can reach a factor 2 from comparison of IRAS and ISO fluxes for objects in two programs.

We also present 12 μm ISOCAM observations of these pairs. The light profiles at this wavelength exhibit shorter disk scale lengths than in the optical. Comparison of H α and 12 μm images of NGC 5545 indicate that ISOCAM images are reliable tracers of star formation.

Subject headings: galaxies: spiral — galaxies: ISM — galaxies: photometry

1. Introduction

Investigating the radiative “energy-balance” within galaxies has recently become more viable (Xu & Helou 1996; Trehella 1998) with the expansion of our ability to view their far-infrared emission. Since dust produces both absorption and thermal emission, its structure and distribution within spiral disks affect how that radiation is released. Both the emission properties of interstellar dust grains and the total mass in grains determine how stellar (optical-UV) light is reradiated as the total infrared flux. If dust exists in very clumpy structures (behaving as large grains with inefficient absorption), inferring dust masses from area-weighted extinction measures would yield underestimates. If a large amount of cold dust exists with FIR emission below the detection limits of ISOPHOT (Lemke et al. 1996), then modified blackbody temperature fitting will yield mass underestimates, as IRAS was shown to have done by using ISOPHOT data evaluate dust masses (Alton, et al. 1998 ; Haas et al. 1998; Krügel et al. 1998). The latter claim is that using IRAS data alone leads to underestimates of dust masses by a factor of 10, because of the IRAS 100 μm cutoff and the contribution of warm dust to the 60 μm measurement. Block et al. (1994) demonstrated that radiative transfer models with B and K' imaging can increase the dust mass estimates of two spiral disks by an order of magnitude over IRAS values.

Debates over the opacity of spirals extend from statistical studies by Holmberg (1958) and Valentijn (1990), using the inclination-surface-brightness tests, to reassessments of that work by Burstein, Willick, & Courteau (1995) and Huizinga (1994). Claims have ranged disks being opaque to being transparent. “Energy-balance” methods (Evans 1995; Xu & Helou 1996) have relied solely on IRAS data with a limiting upper wavelength of 100 μm , while the peak of FIR emission is expected to be between 100 and 300 μm (Evans 1992). Campaigns undertaken to directly measure the opacity within spiral galaxies (White & Keel 1992; Keel & White 1995; White, Keel & Conselice 1996, 1999; ;Gonzales et al. 1998; Domingue, Keel, & White 1999) have shown that moderate extinctions predominate in disks, with spiral arms exhibiting higher levels than interarm regions. These methods exploit the unique opportunity afforded by partially overlapping galaxies. By using the measured extinctions in the B band and converting them to column densities we deduce the total mass of light absorbing dust grains in such overlapping pairs.

A comparison of dust emission and absorption measures is informative since the two complementary techniques have very different sensitivity to dust temperature and clumping. Absorption measures are insensitive to grain temperature, but the mean absorption will be reduced for a given dust mass if the dust is strongly clumped. Conversely, emission measurements are insensitive to dust distribution (as long as the mid- and far-IR optical depth remains small), but they are sensitive to dust temperature, varying as $\sim T^{-5}$ for a

fixed wavelength of observation. The derived masses in both cases scale as H_0^{-2} , so their ratio is distance-independent.

We observed three overlapping galaxy pairs using ISOPHOT mapping from 50-200 μm , along with SCUBA observations up to 2000 μm for two members of the sample. The far-IR measurements were supplemented with 12 μ ISOCAM mapping, to give some insight into the structure of at least the warmer dust, and seek evidence of obscured star formation in the strong dust lanes in these spirals. These data allow us to fit temperatures to the FIR emission and calculate total dust masses based on FIR emission models (Hildebrand 1983; Rowan-Robinson 1992). We then compare dust masses from these two independent methods (FIR/sub-mm emission and directly measured extinction) to determine the role of dust's large scale structure in spiral disks.

2. Observations and Data Reduction

2.1. Sample Selection

The three overlapping-galaxy pairs for this study were chosen from the large survey performed by White, Keel, and Conselice (1999), which surveyed candidates from numerous catalogs to find pairs with the appropriate geometry and symmetry for analysis of the absorption. We believe them to be the apparently largest and brightest partially overlapping spirals within the area of sky accessible to the ISO primary mission.

The proximity in both position and velocity for these pair members virtually guarantees that they are gravitationally bound, either as pairs or as members of small groups. This might introduce the possibility that the spirals we observed are atypical because of interactions. In selecting the sample for this study, we attempted to reduce such effects by eliminating objects showing morphological evidence for tidal distortion, and excluding cases where the presence of a starburst gave hints of externally triggered star formation. Specifically, aside from lack of tidal features in our optical imagery, we can note that the global H α +[N II] equivalent width in NGC 5545 (30 Å) is very close to the median level found for noninteracting Sc galaxies (Kennicutt et al. 1987). Neither our ground-based nor *HST* imagery shows unusual levels of disk star formation, as traced by bright blue knots. Earlier reports of NGC 5091 as “tidally disrupted” (e.g., Smith & Bicknell 1986) appear to rely on interpretation of the NW arm, from photographic plates, as detached from the disk and thus tidally induced. CCD imagery shows that the apparent gap results from the prominent and extensive dust lane crossing the disk in this region, so that this arm structure is not in itself evidence for strong tidal interaction. The radio fluxes of the spirals are all in

typical ranges for the type, when detected at all; there is a weak detection of the nucleus of NGC 5545 (Hummel et al. 1987), while AM1316-241 is undetected in the PMN survey (Griffith et al. 1994) and NGC 5091 does not appear in radio maps of NGC 5090 (which is a classical twin-jet radio galaxy, as noted by Lloyd, Jones, & Haynes 1996). Finally, all these spirals have rather cold colors across the $50\text{-}200\mu\text{m}$ range, another indication that any triggered burst of star formation must be weak in comparison with the steady-state rate. Our intent was to select the most typical spiral galaxies for which this kind of analysis can now be performed. Given the connection between pair membership and the incidence of grand-design spiral patterns (Elmegreen & Elmegreen 1982), and the global spiral patterns shown by each of these galaxies, our results can strictly apply only to grand-design spirals, and it is in this sense that we feel our results may be significantly affected by the proximity of the background galaxies. Such an emphasis is almost unavoidable in using the overlap technique to measure dust extinction.

2.2. Mid-Infrared Observations

Three pairs of galaxies (see Table 1) were observed with ISOCAM (Cesarsky et al. 1996) on board the *Infrared Space Observatory* (ISO) (Kessler et al. 1996) with the LW10 filter($8\text{-}15\mu\text{m}$), which was designed to match the IRAS $12\mu\text{m}$ filter. Each pair was observed in a 2×2 raster mode with a $3''$ pixel scale. Steps of $6''$ were used between each pointing with integration times of 10 seconds each. The final images were 34×34 pixels. The data were reduced with CAM Interactive Analysis (CIA) for dark subtraction, transient removal, flat-fielding and co-addition of frames. The small rastering step size relative to the pairs' apparent sizes did not allow for the production of flat fields from the data. It was necessary to use the flats from the calibration library which can vary from true flats due to changes in the position of the filter wheel (Siebenmorgen et al. 1996). Median background levels were determined from histograms of the outlying regions (see Table 2). The resulting images are in figures 1 through 3.

All six galaxies are detected in the $12\mu\text{m}$ LW10 filter. The elliptical in AM1316-241 is unresolved with a peak to total flux ratio of 0.21, comparable to the LW10 PSF with $3''$ pixels. NGC 5544 is nearly unresolved and all other galaxies in this sample are clearly not point sources. NGC 5091 did not entirely fit into the chosen CAM field-of-view. Its flux was modeled by compositing the image with the symmetric counterpart mirrored about the galaxy's center.

To obtain information on the warm dust distribution, we did conventional ellipse fitting and produced exponential disk models to convolve to the ISOCAM LW10 PSF. Best

(two-dimensional) fits to the ISOCAM data for the three spirals are used to estimate 12 μm exponential scale lengths (see table 2).

2.3. Far-Infrared Observations

The three pairs were observed using the ISOPHOT instrument onboard ISO in P32 mapping mode at 50,100, and 200 μm (see Figure 4). A 3 x 3 rastering with an oversample factor of 3 yielded maps with pixels of 15" x 15". The data were reduced using PHT Interactive Analysis (PIA). Each observation included two Fine Calibration Source (FCS) measurements, one before and after pointings at the target. This was to correct for any detector responsivity fluctuations within the time frame of each observation. Histograms of the resulting images were used to obtain the background level used for subtraction.

Neither AM1316-241 nor NGC 5090/1 was detected at 50 μm . A possible explanation for non-detection is the C100 detector's transient behavior as explained below. These two pairs are detected at 100 and 200 μm and NGC 5545 is detectable at all three wavelengths.

P32 is not currently one of the validated modes of ISOPHOT. This is due to the present inability to calibrate its chopped rastering (Klaas et al. 1998). We apply corrections to calibrate fluxes from this set of data through statistical comparison with IRAS fluxes of these pairs. The present difficulty involves the transient behavior in the C100 detector. Fluxes are underestimated relative to the background because the time scale of the C100 detector to react to the illumination step is comparable to the time between chopper pointings (Tuffs et al. 1996; Laureijs 1999). For point sources this will have a significant affect on the total flux. Our background surface brightness measurements are found to be consistent with the 30% overestimation figure quoted by Alton et al.(1998) in relation to COBE estimations from IRSKY of the same sky backgrounds. This does not mean our fluxes are overestimated, which may differ from the situation for fully resolved targets (Alton et al. 1998). To assist in our calibration efforts we used 20 additional ISOPHOT C100 images at 60 and 100 μm of pairs from the Karachentsev Catalog (KPG), taken in an observing program by J. W. Sulentic. All of these fluxes were contrasted to IRAS ADDSCAN fluxes at 60 and 100 μm for the KPG pairs (Toledo 1998) and our own sample (see Figure 5). A linear fit to the results shows ISOPHOT C100 fluxes to be a factor of 2.2 higher than IRAS fluxes with a small additive offset, which differs for the groupings below and above a measured ISOPHOT flux of 1 Jansky. We apply the multiplicative factor correction of 2.2 to our ISOPHOT C100 fluxes (see Table 3). The affect of transient behavior on the C200 detector is assumed to be smaller (Laureijs 1999). To find a reasonable correction for the C200 data we incorporate our SCUBA flux estimates of AM1316-241

and NGC 5545. Modified blackbody fits to our corrected C100 fluxes and SCUBA flux limits indicate that our C200 data do not require any corrections to be consistent with submillimeter and millimeter observations.

2.4. Submillimeter and Millimeter Observations

We observed AM1316-241 and NGC 5544/5 from 450 μm to 2 mm with the SCUBA instrument (Holland et al. 1999) at the 15m James Clerk Maxwell Telescope (JCMT) on Mauna Kea. The measurements were made on 11 February 1999, with a typical atmospheric $\tau = 1.5$ at 450 μm . The two independent bolometer arrays were used for simultaneous 450 and 850 μm mapping, in the 64-point mode yielding full spatial coverage at both wavelengths. The single-pixel 1.3- and 2-mm detectors were used in a chopped photometric mode centered on each spiral component, with sky chopping at a throw of 120" set to miss the optical and far-infrared extent of the pair members. Flux calibration used Mars, with the same observing modes as for the galaxy data. The mapping fields were centered between the members of each pair, by offset after checking the pointing on AM1316-241 using 3C 279, which also served as a point reference source for mapping the telescope beam. The pointing check on NGC 5544/5 was 1308+326.

In constructing the 450/850 μm maps, noisy bolometers and corrupted integrations were flagged and subsequently ignored. The unflagged measurements were gridded and interpolated into 1" pixels in the α, δ (tangent) plane, using the rotation of the altazimuth telescope coordinates on the sky to fill in blank areas from noisy detectors. Using these maps at 10" resolution gave a $3 - \sigma$ detection of the spiral in AM1316-241 at 21 ± 7 mJy at 850 μm (at the expected coordinates, giving confidence in the detection), and a 450 μm limit of 690 mJy. For NGC 5545, we obtain 3σ upper limits of < 31 mJy (850 μm) and < 450 mJy (450 μm).

The spiral members of these pairs are not well resolved by the JCMT beam at millimeter wavelengths, taking either the optical or ISO imagery as a guide to the extent of the emitting dust. The FWHM of the beam is about 31" and 48" in the two bands, while the scale lengths for exponential-disk fits to the ISOCAM 12 μ images are 2.5" for AM1316-241 and 8.0" for NGC 5545. Accordingly, the measurements at 1.3 and 2 mm used the SCUBA "photometry" detectors in point-source fashion. The following 3σ upper limits were derived: for AM1316-241, $F(1.35 \text{ mm}) < 7.8$ mJy, $F(2 \text{ mm}) < 27$ mJy; for NGC 5545, $F(1.35 \text{ mm}) < 12.8$ mJy and $F(2 \text{ mm}) < 35$ mJy. ISO mapping has shown that for many spirals, scale lengths measured in the optical and mid-IR are useful proxies (at the $\sim 30\%$ level) for the far-IR distribution (Alton et al. 1998, Haas et al. 1998), so we calculated

1.3-2.0 mm beam corrections based on the structures both at optical wavelengths and at 12μ , multiplying these detection limits by the larger of the optical or mid-IR corrections before using them in analysis. These beam corrections are scaling factors of 1.30 (1.15) at 1.35 (2.0) mm for AM1316-241 and 1.5 (1.25) for NGC 5545. The resulting global limits are stringent enough to let us rule out significant emission from very cold dust.

2.5. Supporting Optical and Near-Infrared Imaging

We adopt the absorption measures for AM1316-24 presented by White & Keel (1992). For NGC 5545, we have done a similar analysis using B and I imagery obtained with the prime-focus CCD imager at the 4m Mayall telescope of Kitt Peak National Observatory. The background system NGC 5544 was modelled by fitting elliptical isophotes to the non-overlapping regions and interpolating across the overlap area. The galaxy is slightly asymmetric, so that the usual reflection/subtraction technique employed for elliptical galaxies gives much larger (and systematic) residuals. To subtract light from the foreground system, we employed rotational symmetry after applying a $6''$ median filter to remove bright associations so that residuals due to individual bright clusters and stellar associations would not produce spurious absorption regions. The resulting maps of residual intensity are shown in Fig 6. For regions not disturbed by bright foreground structures, we derive mean values for the interarm region at $r=29''$ $A_B = 0.52, A_I = 0.30$, and for the prominent arm crossing this radius, $A_B = 1.3, A_I = 1.0$. The radial profile of B -band light implies a disk scale length of $12''$, so these measurements apply 2.4 scale lengths from the nucleus.

For NGC 5090/1, we use a B -band image obtained with the CTIO 1.5m, to estimate extinctions within NGC 5091, starting with our usual practice of modelling and subtracting the light distribution of the background elliptical. The prominent dust lane on the NE side of NGC 5091 in fact goes very close to zero intensity after this exercise, demonstrating that the spiral is indeed in front. The typical second step - modelling and subtracting the spiral's own light by symmetry - does not work well in this case, producing unphysical negative flux in much of the overlapped disk. The strong dust lane has no symmetric counterpart, so we are driven to a more uncertain estimate based on the minimum residual intensity in other parts of the disk lane, and just inside its inner edge, at other points with similar radius in the disk plane but essentially no background light. This yields a lower limit $A_B > 2.8$ at the deepest part of the dust lane, about $A_B = 0.6$ at a radius of $19''$, and $A_B < 0.2$ outside the dust lane at $r = 38''$. The disk has substantial local structure, but a compromise exponential scale length of $13.5''$ should be adequate for a dust-mass estimate.

Global estimates of dust mass for these pairs assumed that equal amounts of dust are

in the arm and interarm regions, as suggested by the surface areas and extinctions in the areas that we have measured.

3. Results

3.1. Mid-Infrared

The ISOCAM 12 μm images show us very warm dust emission in the three pairs. The spirals in AM1316-241 and NGC 5544/5 dominate because they are expected to contain more dust and have more gas available for star formation. The elliptical dominates over the spiral in NGC 5090/1, but this early-type galaxy is also a radio galaxy, which suggests an alternate heating source for the dust other than the interstellar radiation field. A convolution of an $\text{H}\alpha$ image of NGC 5545 (Kennicutt et al. 1987) to the ISO LW10 resolution reveals a very good correlation of emission features at these two wavelengths (see Figure 7). This suggests that virtually everything we see in the ISOCAM map is reliable and ties the mid-IR structure to star formation, since $\text{H}\alpha$ is a good indication of star-formation rate (SFR) (Kennicutt 1983). ISOCAM observations of other spirals (Wozniak et al. 1998; Charmandaris et al. 1999) show correlations in the comparison of $\text{H}\alpha$ and mid-IR images. In AM1316-241 and NGC 5544/5 the mid-IR emission scale lengths are shorter than those of the B -band indicating a central predominance of star formation, although the outer disk in NGC 5091 does contain mid-IR emission (Figure 2).

3.2. Extinction Dust Masses

Using radial extinction data for spiral disks, White, Keel & Conselice (1999) empirically show that a declining exponential (with the same scale length as the B -band disk starlight) is a good model for dust distribution in the interarm regions of spirals with about half of a galaxy's dust being located within spiral arms. We calculate column densities of localized regions with measured extinctions and integrate these over the entire disk, adopting the empirical exponential form to derive the total dust mass as seen in extinction.

To generate column densities from the extinction values, we must know the absorption cross section of dust grains at the relevant wavelengths. The size distribution of grains is weighted toward the larger particles of 0.1-0.2 μm (O'Donnell & Mathis 1997) with a classical mean size chosen as 0.1 μm (Hildebrand 1983) and overall density of 2.8 g cm^{-3} . This density is based on an average density of the actual predicted constituent particles of the ISM – graphite having a density of 2.26 g cm^{-3} and silicates such as olivine having

densities of 3.3 g cm^{-3} (Draine & Lee 1984). Another model (O'Donnell & Mathis 1997) argues that the larger grains ($> 0.02 \mu\text{m}$) are composite porous structures with a lower density of $\sim 1.3 \text{ g cm}^{-3}$. Mass estimates are therefore sensitive to the possible fractal nature of grains. Since $0.1 \mu\text{m}$ grains are part of this possibly porous group, we use the porous grain value of 1.3 g cm^{-3} , while noting that masses may be underestimated by a factor of ~ 2 . For particles of this size, absorption efficiencies were calculated by Draine & Lee (1984) using synthesized dielectric functions of “astronomical silicate” and graphite. The efficiencies $Q_{abs} \equiv C_{abs}/\pi a^2$ yield graphite cross sections C_{abs} of $1.6 \times 10^{-11} \text{ cm}^2$ and $6.0 \times 10^{-11} \text{ cm}^2$ for the I and B -bands respectively. Silicate values are $1.3 \times 10^{-10} \text{ cm}^2$ and $2.3 \times 10^{-10} \text{ cm}^2$ for the I and B -bands. Silicate and graphite models, in conjunction with observational evidence, suggest that these species are mixed in a ratio of 1:1 (Mathis, Rumpl, & Nordsieck 1977; Draine & Lee 1984). The cross sections we adopt are the average of the graphite and silicate values. The localized apparent column density is

$$N(r) = \frac{\tau(r)\rho}{C_{abs}}, \quad (1)$$

where τ is our value for the opacity in that region and ρ is the density of the grains, chosen to be 1.3 g cm^{-3} . The central value is

$$N_0 = N(r)e^{r/r_0}, \quad (2)$$

derived from our exponential model where r_0 is the scale length of the disk's B image. We assume the long wavelength emission to have the same distribution as that of the B -band (consistent with the results of Alton et al. 1998).

The total dust mass is found through the integral

$$M_d = 2\pi(b/a)N_0 \int_0^\infty e^{-r/r_0} r dr, \quad (3)$$

which becomes

$$M_d = 2\pi(b/a)N_0 r_0^2, \quad (4)$$

where b/a is the axial ratio of the galaxy. We have taken $H_0 = 75 \text{ km s}^{-1} \text{ Mpc}^{-1}$. Interarm optical depths τ_B and τ_I of AM1316-241 are 0.3 and 0.2 (both at $2.4 r_0$) respectively, while for NGC 5545, τ_B is 0.48 (at $2.4 r_0$), and τ_B is 0.55 (at $1.4 r_0$) for NGC 5091. A final multiplication of the mass by a factor of two is required because we assume that interarm dust represents only half of the dust mass, with the other half in the spiral arms (which fits with the direct extinction measurements cited in the Introduction). Dust masses (see Table 4) are derived from these quantities are $1.6 \times 10^7 M_\odot$ in NGC 5545, $3.9 \times 10^7 M_\odot$ in AM1316-241 and $0.8 \times 10^7 M_\odot$ in NGC 5091 using the B -band opacities. The I -band estimate of the dust mass in AM1316-241 is $4.5 \times 10^7 M_\odot$, consistent with the B -band determination.

3.3. FIR Dust Masses

We consider the most important component of the dust emission by mass, which is the coolest component that is well represented in the spectrum. To a good approximation, we find that the $100 - 2000\mu$ data can be fitted to a single modified blackbody law in each case, with a hotter component (associated with star-forming regions) required only to account for the 50μ emission in NGC 5545.

Single-temperature fitting to the FIR fluxes, with an emissivity law of $\nu^\beta B_\nu(T_d)$ with $\beta = 2$, gives us the total dust mass within these spirals provided there is no significant colder component of their ISM. This modified blackbody emissivity function is a good representative of the FIR emission of dust grains. We choose $\beta = 2$ because it has been shown to fit the spectrum of ISO data on spirals (Krügel et al. 1998) and our limited number of data points are not suited to constraining this parameter. Temperature errors were estimated using a Monte Carlo approach, the modified blackbody fits were applied to points with gaussian distributions about the measured fluxes using an error of 30% for ISOPHOT data (as in Table 3) and the SCUBA detection error at $850\mu\text{m}$ in the case of AM1316-241 (Table 3). This gives us a mean temperature and $1-\sigma$ errors (see Table 4). In AM1316-241 we are able to fit fluxes at 100 , 200 , and $850\mu\text{m}$. NGC 5091 and NGC 5545 have fits only to 100 and $200\mu\text{m}$ data points with very useful upper limits at sub-mm and millimeter wavelengths for NGC 5545. The FIR flux in these three pairs is dominated by the foreground spiral since the background galaxy in each case is an early type E or S0 (see table 1) with the possible exception of NGC 5090/1 in which the elliptical is a radio galaxy that is dominant at $12\mu\text{m}$. The dominance of spirals in the IR is expected as a result of early-type galaxies' deficiencies in gas and dust content and observationally confirmed for IR luminous pairs of different Hubble types (Bushouse, Telesco, & Werner 1998) and our own ISOCAM observations, excluding NGC 5090/1, presented in this paper. Resulting temperatures of 21 K therefore represent those of a cold component of the dusty spirals in AM1316 and NGC 5545. Temperatures derived from IRAS $60\mu\text{m}$ and $100\mu\text{m}$ fluxes are 29 K and 25 K respectively. The derived temperature for NGC 5091 is 22 K , which agrees with the IRAS temperature within the errors.

An additional warmer component of dust is required to fit the $50\mu\text{m}$ flux of NGC 5545. We add a 47 K dust population which keeps the added flux within the errors and fits both ISOPHOT $50\mu\text{m}$ and IRAS $25\mu\text{m}$ data points (See Figure 8). The upper limit on the AM1316 $50\mu\text{m}$ emission allows for a similar warm dust component, but the possible contribution of the early-type member of the pair to the IRAS $25\mu\text{m}$ flux would cause the derived temperature to be too high. If none of the emission is from the elliptical, we can impose a strict upper limit of 60 K to this warm dust. The masses of the 40 K and

above components as calculated in the manner below are only 1% of the total dust mass and are relatively insignificant. The temperature fit in NGC 5545 strongly depends on the reliability of the 200 μm flux. A detection at 850 μm would better constrain the fit below the upper limit at that wavelength.

Interpreting the FIR emission as a total dust mass requires a understanding of the grain composition within spiral disks. We consider two models for this emission. The simple single grain model for mass determination (Hildebrand 1983) is:

$$M_d = \frac{4a\rho D^2}{3} \frac{F_\nu}{Q_\nu B_\nu(T_d)}, \quad (5)$$

where $\rho = 3 \text{ g cm}^{-3}$ is the grain density, $a = 0.1\mu\text{m}$ is the grain size, D is the galaxy distance ($H_0 = 75 \text{ km s}^{-1} \text{ Mpc}^{-1}$), F_ν is the measured flux, $B_\nu(T_d)$ is the Planck function, and Q_ν is the grain emissivity where

$$Q_\nu = \frac{3}{1300} \left(\frac{\nu}{\nu_{125\mu\text{m}}} \right)^2, \quad (6)$$

and $\nu_{125\mu\text{m}}$ is the frequency corresponding to 125 μm . This model has been applied to the 200 μm ISOPHOT fluxes and 100 μm IRAS fluxes of several nearby spiral galaxies by Alton et al. (1998) to estimate masses at $3 - 10 \times 10^7 M_\odot$. When applied to the three pairs our sample, this model predicts dust masses (see table 4) of $0.1 - 2.6 \times 10^7 M_\odot$.

A more complex model (Rowan-Robinson 1992), which takes into account different grain sizes and distributions, is based on the behavior of the infrared cirrus. This cirrus model separates cirrus and starburst components in galactic emission and can be well fit by the $\nu^2 B_\nu(T_d)$ emissivity. The parameters of this model require a temperature and a 100 or 800 μm flux along with the distance of each galaxy. The scaling factor $\log(M_d/S_{100}D^2)$ is approximately 3 for temperatures of 21 - 22 K. We derive dust masses (see Table 4) which are similar to those of the Hildebrand (1983) model and range from $0.1 - 3.2 \times 10^7 M_\odot$.

4. Summary and Discussion

Far-infrared photometry from 50-2000 μm , when used together with extinction maps of spiral disks, reveals the nature of the dusty structures within those galaxies. Grain models, plus ISOPHOT FIR and SCUBA sub-mm/mm observations yield dust masses of $1-3 \times 10^7 M_\odot$ for NGC 5545 and AM1316-241. Extinction measures in these overlapping spiral galaxies lead to comparable mass estimates.

In NGC 5545, our sub-mm flux limits restrict any significant mass of undetected dust to $T < 7 \text{ K}$, while $T < 10 \text{ K}$ for any undetected dust in AM1316, i.e. the dust mass of these two

galaxies can only increase by a factor of 2 or more if there exists a significant contribution below these temperatures. A lack of evidence from COBE for grain temperatures below 13 K in the Milky Way (Lagache et al. 1998) argues for an upper limit of twice the tabulated dust mass unless these galaxies contain a very different type of dust grain population than the Milky Way.

In NGC 5091, the large difference in dust mass resulting from the two methods permits a larger fraction of cold dust to exist, but the incomplete data set for this pair limits the interpretation of the results and the possible far-IR contamination by the radio elliptical may affect the temperature fitting.

Because the dust masses derived from extinction measures are slightly higher than those derived from FIR emission, dust cannot be hiding in clumpy structures. Small opaque structures would not have a strong affect on area weighted absorption measures. In such a case, absorption measures would be interpreted as lower dust masses than FIR models would predict. We do not see any evidence for this possibility and it is unlikely that any significant amount of dust exists in opaque structures. Small, opaque dust structures at $T < 10$ K cannot be ruled out, but there seems no physical motivation for that option.

Given the uncertainties in each of these calculations, their agreement is striking, and suggests that both techniques observe essentially all the dust in typical spirals, in as far as these gravitationally pair-bound spirals can be considered typical of grand-design spiral galaxies.

We thank G. Moriarty-Schieven for assistance with the JCMT observations. The ISOPHOT data presented in this paper were reduced using “PIA”, which is a joint development by the ESA Astrophysics Division and the ISOPHOT consortium. The ISOCAM data presented in this paper were analysed using “CIA”, a joint development by the ESA Astrophysics Division and the ISOCAM Consortium. The ISOCAM Consortium is led by the ISOCAM PI, C. Cesarsky, Direction des Sciences de la Matiere, C.E.A., France. D.D. greatly appreciates the training received using these data analysis packages while attending the Les Houches summer school entitled “Infrared Space Astronomy Today and Tomorrow”. We thank J.W. Sulentic for the use of additional ISOPHOT data to assist in P32 corrections. This work was supported by NASA/ISO grant NAG 5-3336.

REFERENCES

Alton, P.B., Trehewella, M., Davies, J.I., Evans, R., Bianchi, S., Gear, W., Thronson, H., Valentijn, E. & Witt, A. 1998, A&A, 335, 807

Block, D. L., Witt, A. N., Grosbol, P., Stockton, A., Moneti, A., 1994, A&A, 288, 383

Burstein, D., Willick, J., & Courteau, S. 1995, in *The Opacity of Spiral Disks*, eds. J.I. Davies & D. Burstein, (Dordrecht: Kluwer), p.73

Bushouse, H. A., Telesco, C. M., & Werner, M. W. 1998, AJ, 115, 938

Cesarsky, C. et al. 1996, A&A, 315, L32

Charmandaris, V. 1999, A&A, 341, 69

Domingue, D. L., Keel, W. C., & White, R. E. III 1999, ApJ, submitted

Draine, B. T., & Lee, H. M. 1984, ApJ, 285, 89

Elmegreen, D.M. & Elmegreen, B.G. 1982, MNRAS, 201, 1021

Evans, Rh., 1992, Ph.D. Thesis University of Wales Cardiff

Evans, Rh., 1995, in *The Opacity of Spiral Disks*, eds. J.I. Davies & D. Burstein, (Dordrecht: Kluwer), p.281

Griffith, M. R., Wright, A. E., Burke, B. F., & Ekers, R. D. 1994 ApJS, 90, 179

Gonzales, R. et al. 1998, ApJ, 506, 152

Haas, M., Lemke, D., Stickel, M., Hippelein, H., Kunkel, M., Herbstmeier, U. , & Mattila, K. 1998, A&A, 338, L33

Hildebrand, R. H. 1983, QJRAS, 24, 267

Holland, W. S., Robson, E. I., Gear, W. K., Cunningham, C. R., Lightfoot, J. F., Jenness, T., Ivison, R. J., Stevens, J. A., Ade, P.A.R., Griffin, M. J., Duncan, W.D., Murphy, J.A., & Naylor, D.A., 1999, MNRAS, 303, 659

Holmberg, E. 1958, Medd. Lunds Astr. Obs, ser 2, no. 136

Huizinga, J. E. 1994, Ph.D. thesis, Rijksuniversiteit Groningen

Hummel, E., van der Hulst, J. M., Keel, W. C., & Kennicutt, R. C. 1987, A&AS, 70, 517

Keel, W. C. & White, R. E. III 1995, in *The Opacity of Spiral Disks*, eds. J.I. Davies & D. Burstein, (Dordrecht: Kluwer), p.167

Kennicutt, R. C., 1983, ApJ, 272, 54

Kennicutt, R. C., Keel, W. C., van der Hulst, J. M., Hummel, E., Roettiger, K. A., 1987, AJ, 93, 1011

Kessler M.F. et al., 1996, A&A, 315, L27

Klaas, U., Laureijs, R. J., Radovich, M., & Schulz, B. 1998, "ISOPHOT Calibration Accuracies", ESA, SAI/98-092/Dc

Krügel, E., Siebenmorgen, R., Zota, V., & Chini, R. 1998, A&A, 331, L9

Lagache, G., Abergel, A., Boulanger, F., Puget, J.-L., 1998, A&A, 333, 709

Laureijs, R. J. 1999, private communication

Lemke, D., et al. 1996, A&A, 315, L64

Lloyd, B.D., Jones, P.A., & Haynes, R.F. 1996, MNRAS, 279, 1197

Mathis, J. S., Rumpl, W., & Nordsieck, K. H. 1977, ApJ, 217, 425

O'Donnell, J. E., & Mathis, J. S. 1997, ApJ, 479, 806

Rowan-Robinson 1992, MNRAS, 258, 787

Siebenmorgen, R., Starck, J. L., Cesarsky, D. A., Guest, S., & Sauvage, M. 1996 , "ISOCAM Data Users Manual", ESA, SAI/95-222/Dc

Smith, R. M., Bicknell, G. V. 1986, ApJ, 308, 36

Toledo, H. M. H. 1998, PhD Thesis Universidad Nacional Autonoma De Mexico

Trewhella, M. 1998, MNRAS, 297, 807

Tuffs, R. J., et al. 1996, A&A, 315, L149

Valentijn, E. A. 1990, Nature, 346, 153

White, R. E. III, & Keel, W. C. 1992, Nature, 359, 129

White, R. E. III, Keel, W. C., & Conselice, C. J. 1996, in *New Extragalactic Perspectives in the New South Africa*, ed. D. Block & M. Greenberg, (Dordrecht: Kluwer), p. 114.

White, R. E. III, Keel, W. C., & Conselice, C. J. 1999, ApJ, submitted

Wozniak, H., Friedli, D., Martinet, L., Pfenniger, D. 1998, A&A, 330, L5

Xu, C., & Helou, G. 1996, ApJ, 456, 163

Figure Captions

Fig. 1.— B band HST image of AM1316-241 (left) and ISOCAM LW10 image (right) of the same field. The elliptical is a point source to ISOCAM.

Fig. 2.— B band CTIO image of NGC 5090/1 (left) and ISOCAM LW10 image (right) of the inset field-of-view. The foreground disk exhibits low emission.

Fig. 3.— B image of NGC 5544/5 (left) with masked background and ISOCAM LW10 image (right) of the same field. The SB0 (NGC 5544) only appears as a faint nucleus at $12 \mu\text{m}$. The interarm separation in the North-East spiral arm is noticeable in the ISOCAM image.

Fig. 4.— ISOPHOT P32 maps of (left to right) AM1316, NGC 5090/1, NGC5544/5 at (top to bottom) 50, 100 & 200 μm .

Fig. 5.— A comparison of IRAS flux estimates vs. fluxes from 20 ISOPHOT P32 maps of pairs at 60 & 100 μm . Plus signs & asterisks represent pairs from an ISOPHOT observing program by J.W. Sulentic at 60 & 100 μm respectively. Diamonds represent the three pairs in this paper which were observed at 100 μm . The best fit slope is 2.2, suggesting the needed correction to these ISOPHOT data.

Fig. 6.— Residual intensity maps ($e^{-\tau}-1$) in B (top) and I (bottom) of the overlap region in NGC 5544/5. Dark regions indicate higher extinction.

Fig. 7.— An $\text{H}\alpha$ image of NGC 5545, the same image convolved to the PSF of ISOCAM LW10, and the ISOCAM LW10 image for comparison. Every structure in the CAM image can also be seen in the convolved image including the N-E arm, S-W arm and the SB0 nucleus.

Fig. 8.— The temperature fits of AM1316-241 and NGC 5545. ISOPHOT (50, 100, 200 μm) data and SCUBA JCMT (450-2000 μm) data are represented by boxes and IRAS 25 μm data are diamonds. The sum of the 47 K and 21 K fits to the spectrum of NGC 5545 is displayed as the dashed line.

Table 1: Properties of Galaxy Pairs

Foreground	R.A.(J2000)	Decl.(J2000)	Hubble type	R_{25}^B	R_0^B	cz^a
Background	[h m s]	[$^{\circ}$ ' "]		(arcsec)	(arcsec)	(km/s)
AM1316-241	13 19 33.1	-24 29 27	Sbc	37.5	9	10365
...	13 19 31.8	-24 29 01	E0	9703
NGC 5091	13 21 18.5	-43 43 19	Sb	53.4	13	3365
NGC 5090	13 21 12.8	-43 42 16	E2	3257
NGC 5545	14 17 04.9	+36 34 29	SA(s)bc	37.8	12	3302
NGC 5544	14 17 02.5	+36 34 17	(R)SB(rs)0/a	3292

^aGalactic Standard of Rest.

Table 2: Mid-IR Fluxes

Galaxy	Other Names	F_{LW10}	$R_0^{12\mu m}$
		(mJy)	(arcsec)
AM1316-241	ESO-LV 5080451	28.0	2.5
...	ESO-LV 5080450	6.9	...
NGC 5091	...	7.1	6.6
NGC 5090	...	33.1	...
NGC 5545	...	58.9	8.0
NGC 5544	...	1.5	...

Table 3: FIR and Sub-mm Fluxes

Galaxy	F_{50}^{a} (Jy)	F_{100}^{a} (Jy)	F_{200} (Jy)	F_{450} (mJy)	F_{850} (mJy)	F_{1350} (mJy)	F_{2000} (mJy)
AM1316-241	<0.9	1.1	0.6	<690	21±7	<7.8	<27.1
NGC 5091	<0.2	0.7	0.6
NGC 5545	0.9	2.0	2.0	<450	<31	<12.8	<35.5

^aISOPHOT fluxes are corrected values; 50 and 100 μm values are multiplied by a factor of 2.2

Table 4: Dust Masses and Temperatures

Galaxy	T (K)	Extinction M_d^a ($10^7 M_\odot$)	FIR M_d^b ($10^7 M_\odot$)	FIR M_d^c ($10^7 M_\odot$)
AM1316-241	21.0 ± 1.7	3.9	3.2	2.6
NGC 5091	22.1 ± 3.9	0.8	0.1	0.1
NGC 5545	21.0 ± 3.5	1.6	0.6	0.5

^aNon-Porous grain densities would increase extinction masses by a factor of ~ 2 (see §3.2)

^bCirrus Model

^cAverage grain Model